mater.scichina.com link.springer.com

Published online 9 August 2021 | https://doi.org/10.1007/s40843-021-1732-1
Sci China Mater 2022, 65(1): 131–138

Ru-Co-Mn trimetallic alloy nanocatalyst driving bifunctional redox electrocatalysis

Shan Liu, Erhuan Zhang*, Xiaodong Wan, Rongrong Pan, Yuemei Li, Xiuming Zhang, Mengyao Su, Jia Liu* and Jiatao Zhang*

ABSTRACT **Water electrolysis is one of the most promising approaches for producing hydrogen. However, it has been hindered by the sluggishness of the anodic oxygen evolution reaction. In this work, we fabricated Ru-Co-Mn trimetallic alloy nanoparticles on N-doped carbon support (RuCoMn@NC) *via* the pyrolysis-adsorption-pyrolysis process using ZIF-67 as a precursor. The RuCoMn@NC catalyst exhibited excellent electrocatalytic performance for the hydrogen evolution reaction (HER) over a wide range of pH and glucose oxidation reaction in alkaline media. It showed exceptional HER activity in alkaline medium, superior to that of the commercial Pt/C catalyst (20 wt%), and good electrochemical stability. Further, a two-electrode alkaline electrolyzer pairing RuCoMn@NC as both cathode and anode was employed, and only a cell voltage of 1.63 V was required to attain a current density of 10 mA cm^{-2} in glucose electrolysis, which is about 270 mV lower than that in the overall water-splitting electrolyzer. This paper provides a promising method for developing efficiently bifunctional electrocatalysts driving redox electrocatalysis, and it would be beneficial to energy-saving electrolytic H_2 production.**

Keywords: Ru-Co-Mn trimetallic alloy, HER, glucose oxidation reaction, redox electrocatalysis

INTRODUCTION

The energy crisis is one of the critical issues limiting human development, and the key to solving the problem is the design and synthesis of high-performance catalytic materials for clean energy generation and conversion [1]. Hydrogen is considered a clean energy source that can replace fossil fuels in the future. It has high combustion calorific value and high weight energy density [2]. Its combustion product is water, and the energy conversion process is clean and pollution-free. Significantly, hydrogen can be made from water through electrolytic water splitting, which is widely considered as an environmentally friendly and sustainable technology for producing clean energy. Water electrolysis involves two semi-reactions: hydrogen evolution reaction (HER) and oxygen evolution reaction (OER). However, as a key step for water decomposition, OER has slow reaction kinetics and high overpotential, which hinder the progress of the overall water splitting. The major energy loss in water electrolysis is attributed to the sluggishness of anodic OER [3]. Recently, some researchers have proposed hydrogen production *via* oxidation reactions of substances, such as hydrazine [4], urea [5], and 5-hydroxymethyl furfural [6], instead of anodic OER. The voltage input of the electrolytic cell can be reduced by anodic organic molecular oxidation, which is more favorable in thermodynamics than OER [6–9]. The theoretical thermodynamic potential of glucose oxidation to gluconate is much smaller than that of OER (1.23 V) [10], making it an attractive substitute for OER in hydrolysis [11,12]. It is vital to design electrode materials with high catalytic activity and stability that can drive redox reactions to greatly reduce the overpotential of cathode and anode, thereby decreasing the energy consumption of industrial electrocatalytic production of hydrogen [13,14].

Currently, platinum (Pt) is the most commonly used commercial HER electrocatalyst owing to its excellent catalytic performance. However, its large-scale commercialization is limited by its high cost, low abundance, and poor durability [15]. In the past few decades, several transition-metal (TM)-based catalysts, including their carbides [16], nitrides [17], sulfides [18], phosphides [19,20], oxides [21], borides [22], and heterogeneous heteroatomic (N, P, S, B) [23–26] doped carbon materials have demonstrated good capacity for driving HER. They are promising alternative catalysts for HER owing to their low cost, high efficiency, and abundance. Nevertheless, the catalytic performance of TM-based catalysts is still unsatisfactory compared with that of Pt-based electrocatalysts. Recently, metal alloy catalysts containing small amounts of noble metals have attracted attention owing to their good corrosion resistance in acidic and alkaline environments [27]. Alloying of transition metals with relatively cheap non-Pt noble metals can combine their distinct advantages, and thus, the synthesized catalyst exhibits a high performance-to-price ratio. Besides, metal-organic frameworks (MOFs) and other coordination compounds have recently gained wide attention as precursors for preparing carbon-based electrocatalysts with high electrical conductivity and uniform distribution of active sites [28–30]. The resulting N-doped carbon matrix can afford a good platform to disperse alloying metal particles.

Herein, we developed a Ru-Co-Mn ternary alloy supported on N-doped porous carbon polyhedral (RuCoMn@NC), which can

School of Materials Science & Engineering, Beijing Key Laboratory of Construction-Tailorable Advanced Functional Materials and Green Applications, Experimental Center of Advanced Materials, Beijing Institute of Technology, Beijing 100081, China
* Corresponding authors (emails: zhangjt@bit.edu.cn (Zhang J); liujia86@bit.edu.cn (Liu J); erhuanzh@163.com (Zhang E))

function as a highly efficient bifunctional electrocatalyst for both HER and glucose oxidation reaction (GOR). Owing to the alloying effect with favorable composition, abundant mesoporous structure, large surface area, and conductive N-doped carbon matrices, the optimized RuCoMn@NC showed excellent HER performance under all pH conditions and good GOR performance in alkaline media. The RuCoMn@NC catalyst displayed an overpotential of 38 mV at 10 mA cm^{-2} in 1.0 mol L^{-1} KOH, exceeding that of the commercial 20 wt% Pt/C catalyst (64 mV). Moreover, the overpotentials were 119 and 90 mV to deliver a current density of 10 mA cm^{-2} in 0.5 mol L^{-1} H_2SO_4 and 1.0 mol L^{-1} phosphate buffer saline (PBS). An electrolyzer with RuCoMn@NC electrode as both HER cathode and GOR anode required only an applied voltage of 1.63 V for an electrolysis current density of 10 mA cm^{-2}, which was 270 mV less than that for water splitting.

EXPERIMENTAL SECTION

Synthesis of ZIF-67

The ZIF-67 particles were synthesized following the procedure reported in a previous study [31] with some modifications. The process was as follows: $Co(NO_3)_2{\cdot}6H_2O$ (1.726 g, 6 mmol) and 2-methylimidazole (2-MeIm, 1.970 g, 24 mmol) were, respectively, dissolved in 30 mL of methanol to form clear solutions; the prepared 2-MeIm solution was quickly poured into a Co^{2+}-containing solution and stirred for 10 s; the mixed solution was maintained at room temperature for 20 h; the resulting ZIF-67 precipitates were collected by centrifugation, washed with ethanol for several times, and dried at 60°C in the vacuum oven for 24 h.

Synthesis of the Co@NC

The as-synthesized ZIF-67 was poured into a tube furnace and heated to 400°C at a ramp rate of 2°C min^{-1} and kept for 2 h in a 5 vol% H_2/Ar flow. The temperature was then raised to 700°C with a ramp rate of 2°C min^{-1} and maintained at the temperature for another 2 h. The furnace was then cooled naturally to room temperature (25°C) to obtain Co@NC black powder.

Synthesis of RuCoMn@NC

For RuCoMn@NC, 75 mg of the as-prepared Co@NC nanoparticles (NPs) were dispersed in 5 mL of *n*-hexane and ultrasonicated at room temperature for 10 min to get a homogeneous dispersion. Then, 200 μL of a $RuCl_3{\cdot}3H_2O$ aqueous solution (1.55 mol L^{-1}) and 200 μL of a $MnCl_2{\cdot}4H_2O$ aqueous solution (1.55 mol L^{-1}) were added to the above solution dropwise and stirred for 2 h. Co@NC with the adsorbed Ru^{3+} and Mn^{2+} was collected by centrifugation and then freeze-dried for 24 h. The dried sample was placed in a tube furnace and heated to 500°C at a ramp rate of 2°C min^{-1} and kept for 2 h in a 5 vol% H_2/Ar flow. The same synthetic procedure was employed to synthesize RuCo@NC without using the $MnCl_2{\cdot}4H_2O$ aqueous solution. For RuCoFe@NC, RuCoNi@NC, and RuCoCu@NC, the $MnCl_2{\cdot}4H_2O$ aqueous solution was replaced with $Fe(NO_3)_3{\cdot}9H_2O$, $Ni(NO_3)_2{\cdot}6H_2O$, and $CuCl_2{\cdot}2H_2O$ aqueous solutions, respectively.

Catalyst characterization

Low-resolution transmission electron microscopy (TEM) images of the samples were obtained using HITACHI H-7650 (accelerating voltage of 80 kV) electron microscope. High-resolution TEM (HR-TEM) and element mapping were performed using an FEI Tecnai G2 F20 S-Twin (acceleration voltage of 200 kV) electron microscope equipped with an X-ray energy-dispersive spectroscopy detector. The X-ray diffraction (XRD) patterns were collected using a Bruker D8 multiply crystals X-ray diffractometer (6° min^{-1}). X-ray photoelectron spectroscopy (XPS) was performed on a PerkinElmer Physics PHI 5300 spectrometer. The surface areas and pore-size distributions were analyzed by N_2 adsorption-desorption isotherms using a Make ASAP 2460 instrument. Raman spectroscopy was measured using a Renishaw inVia Raman spectrometer and 514-nm excitation wavelength.

Electrochemical measurements

All electrochemical measurements were conducted on a CHI 760E electrochemical workstation with a standard three-electrode setup. The samples were tested on a rotating disk electrode (RDE; 0.196 cm^2 in area) as the working electrode with Ag/AgCl and Pt wire as the reference and counter electrodes, respectively. The electrochemical measurements for all samples (RuCoMn@NC, RuCo@NC, etc.) were performed under the same test conditions. Typically, 2 mg of catalyst was dispersed in a mixture of 0.05 mL of Nafion (5 wt%), 0.20 mL of ethanol, and 0.25 mL of distilled water and sonicated for 30 min to form an ink solution. Then, 10 μL of the ink was loaded onto the RDE surface (loading ~0.2 mg cm^{-2}) and dried at room temperature. The HER electrocatalytic activity of the samples was examined by obtaining the polarization curves using linear sweep voltammetry (LSV) with a scan rate of 5 mV s^{-1} at a rotational speed of 1600 r min^{-1} in 1.0 mol L^{-1} KOH, 0.5 mol L^{-1} H_2SO_4, and 1.0 mol L^{-1} PBS solutions, respectively. Electrochemical impedance spectroscopy (EIS) was performed with alternating current (AC) voltage of 5 mV amplitude in the frequency range of 0.05–100,000 Hz. Stability tests were performed by long-term chronoamperometric *i-t* curves under a constant voltage. The Tafel slope was obtained by linear fitting according to the Tafel equation ($\eta = a + b\log j$, where η is the overpotential, b is the Tafel slope, and j is the current density). The electrochemical double-layer capacitance (C_{dl}) was determined by cyclic voltammetry (CV), which was performed at a voltage range of 0.88–0.98 V (*vs.* reverse hydrogen electrode (RHE)) and scan rates of 10–60 mV s^{-1} in 1.0 mol L^{-1} KOH. The electrocatalytic activity of glucose oxidation of the samples was evaluated by CV (scan rate of 10 mV s^{-1}) and amperometry (*i-t*). The polarization curve potentials were obtained with *iR* compensation and converted to RHE using Equation (1).

$$E_{RHE} = E_{Ag/AgCl} + 0.059pH + E^{0}_{Ag/AgCl} \left(E^{0}_{Ag/AgCl} = 0.197V\right). \quad (1)$$

For alkaline water/glucose electrolysis, the catalyst ink was prepared following the same procedure for preparing the working electrodes, and 10 μL of the catalyst ink was uniformly coated on the surface of a glassy carbon electrode (GCE), which was used as both cathode and anode. 1.0 mol L^{-1} KOH with 0.3 mol L^{-1} glucose solution was used as the anode chamber electrolyte and 1.0 mol L^{-1} KOH solution was added to the cathodic compartment. The LSV curve was performed at a scan rate of 5 mV s^{-1}.

RESULTS AND DISCUSSION

Synthesis and characterizations of RuCoMn@NC

Fig. 1a illustrates the preparation process for Ru-Co-Mn alloy NPs on the N-doped carbon support. First, the rhombic dodecahedron-shaped ZIF-67 precursor was successfully synthesized (Fig. 1b and Fig. S1). The ZIF-67 was pyrolyzed under H_2/Ar atmosphere. The carbonized product was denoted as Co@NC, which retained the rhombic dodecahedron shape with densely distributed Co particles (Fig. 1c). The synthesized Co@NC was dispersed in *n*-hexane, and an aqueous solution containing Ru^{3+} and Mn^{2+} was dropped into the homogeneous dispersion and stirred to obtain Co@NC impregnated with Ru^{3+} and Mn^{2+} (denoted as Co@NC/Ru^{3+} and Mn^{2+}). The obtained sample was freeze-dried and thermally treated under H_2/Ar atmosphere to obtain RuCoMn@NC. The content of ruthenium was 2.15 at%, according to the XPS results (Table S1). In comparison, RuCo@NC was synthesized using the same method without the addition of Mn^{2+}. The TEM images of RuCoMn@NC and RuCo@NC (Fig. 1d and Fig. S2) show similar size and shape as those of Co@NC, and there were metallic NPs homogeneously embedded on the carbon support. The HR-TEM image of RuCoMn@NC (Fig. 1e) shows clear lattice fringes with an inter-fringe distance of 0.235 nm located between the {211} lattice spacing of MnCo (0.257 nm) and RuCo (0.083 nm). The analysis revealed that the as-prepared catalyst was loaded with the Ru-Co-Mn trimetallic alloy. High-angle annular dark-field scanning TEM (HAADF-STEM) and the corresponding elemental mapping images (Fig. 1f) show that Ru, Co, Mn, C, and N elements are homogeneously distributed, which indicates that the RuCoMn alloy NPs are uniformly embedded on the N-doped carbon polyhedra.

Fig. 2a shows the XRD spectra of Co@NC, RuCo@NC, and RuCoMn@NC. A diffraction peak at 30° was observed for the three samples, indicating the presence of carbon. Diffraction peaks at 51.8° and 60.2° for Co@NC are ascribed to the (111) and (200) planes of the cubic phase of metallic Co (JCPDS No. 15-0806), indicating the existence of Co metal. For the RuCo@NC, the diffraction peaks are close to the standard Ru diffraction peaks (JCPDS No. 06-0663), but they all shift toward higher angles, suggesting a change in lattice spacing due to the formation of RuCo alloy. The diffraction peaks of RuCoMn@NC are located between those of standard Ru, Co, and Mn (JCPDS No. 32-0637), indicating the successful fabrication of highly crystalline alloyed RuCoMn NPs, which is consistent with the HR-TEM results (Fig. 1e). The elemental composition and electronic states of the samples were further analyzed by XPS. The peaks at about 484.2 and 462.0 eV, corresponding to Ru $3p_{1/2}$ and Ru $3p_{3/2}$ (Fig. 2b), confirm Ru metal in both RuCo@NC and RuCoMn@NC [32]. The Co 2p spectrum of RuCoMn@NC (Fig. 2c) indicates that the presence of Co^0 (778.7 and 793.8 eV) [33,34]. The peaks at 781.4 and 797.3 eV with shakeup satellites (786.4 and 803.1 eV) correspond to Co–N_x species [34–36]. RuCo@NC and Co@NC show the same type of deconvolution peak. However, compared with those of Co@NC, the peak positions of RuCo@NC and RuCoMn@NC shift positively, which indicates electron transfer from Co to Ru or Mn [37]. The Mn 2p spectrum (Fig. 2d) reveals the presence of metallic (653.7 and 641.3 eV) and ionic (642.6 eV) Mn, and the peak centered at 647.0 eV is attributed to the shakeup satellite peak [38]. The pore structures for the RuCo@NC and RuCoMn@NC catalysts were characterized by N_2 adsorption-desorption measurements. The Brunauer-Emmett-Teller (BET) surface area of RuCoMn@NC is 110.35 $m^2 g^{-1}$ (Fig. 2e), which is higher than that of RuCo@NC (87.86 $m^2 g^{-1}$) (Fig. S3), implying that the formation of the trimetallic alloy with the introduction

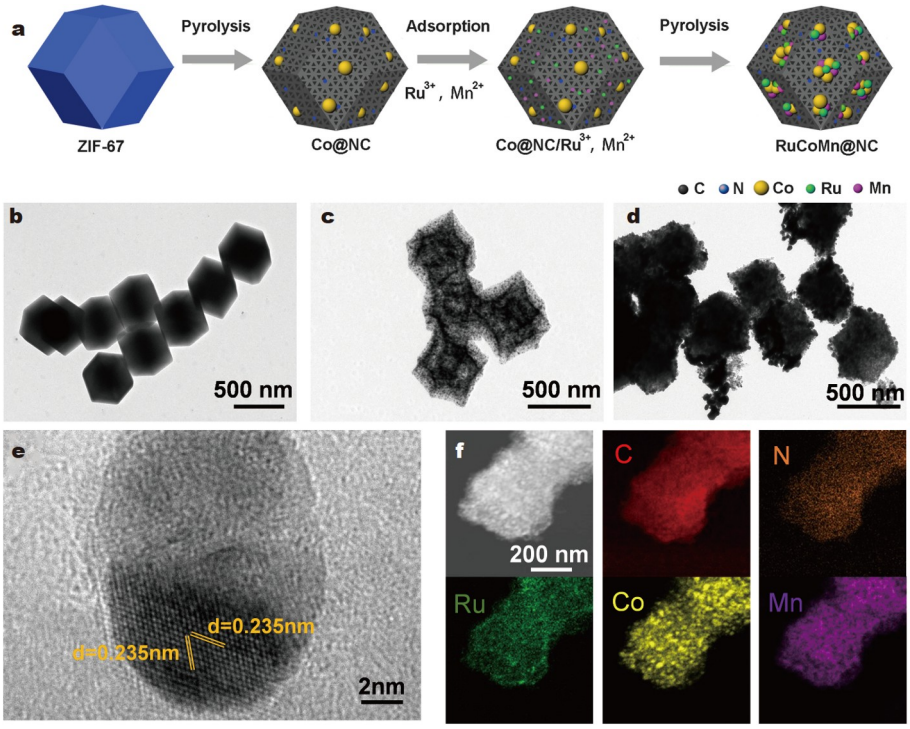

Figure 1 (a) Schematic illustration of the preparation process for RuCoMn@NC. TEM images of (b) ZIF-67, (c) Co@NC, and (d) RuCoMn@NC. (e) HR-TEM image of RuCoMN@NC. (f) HAADF-STEM and the corresponding elemental mapping images of RuCoMn@NC.

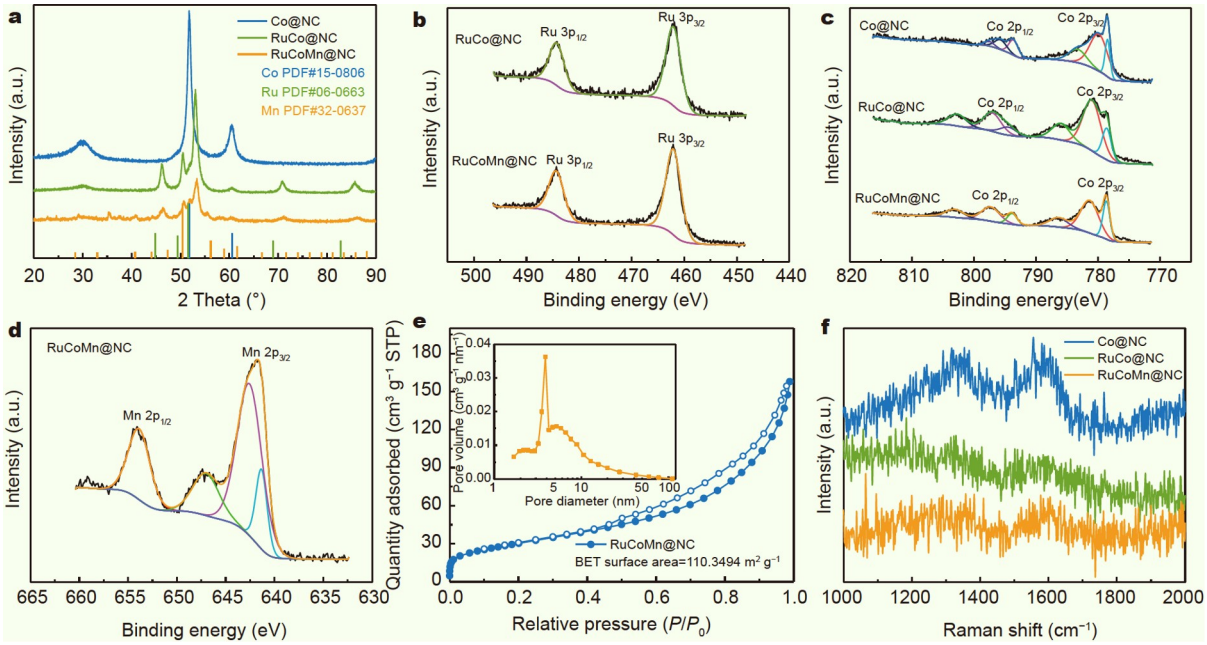

Figure 2 (a) XRD patterns of Co@NC, RuCo@NC, and RuCoMn@NC. XPS spectra of (b) Ru 3p, (c) Co 2p, and (d) Mn 2p of RuCoMn@NC. (e) N_2 adsorption-desorption isotherm and the pore-size distribution of RuCoMn@NC. (f) Raman spectra of Co@NC, RuCo@NC, and RuCoMn@NC.

of Mn results in a higher surface area. Moreover, the pore-size distribution curves (inset of Fig. 2e) indicate the porosity of the RuCoMn@NC catalyst. The porosity and high surface area of the RuCoMn@NC catalyst enhance charge and mass transport during electrocatalysis [39]. The Raman spectrum shows two peaks at ~1336 and 1595 cm^{-1}, representing the D band (defective carbon) and G band (graphitic carbon), respectively (Fig. 2f) [40].

HER of RuCoMn@NC catalyst

The HER catalytic performance of the as-synthesized RuCoMn@NC catalyst was first tested in a 1.0 ml L^{-1} KOH aqueous solution. For comparison, several reference samples, including Co@NC, RuCo@NC, and the commercial 20% Pt/C, were also examined. Fig. 3a shows the *iR*-corrected LSV curves of all samples at 1600 r min^{-1} with 1 mV s^{-1}. RuCoMn@NC exhibits the highest HER activity with a low overpotential (η) of only 38 mV at a current density of 10 mA cm^{-2}, which is lower than that of Co@NC (215 mV), RuCo@NC (67 mV), and even Pt/C (64 mV). The Tafel slope was obtained to investigate the reaction kinetics during HER (Fig. 3b). The Tafel slope of RuCoMn@NC is approximately 34 mV dec^{-1}, which is less than that of Co@NC (169 mV dec^{-1}), RuCo@NC (53 mV dec^{-1}), and Pt/C (35 mV dec^{-1}). This indicates that the Volmer-Tafel mechanism is the HER pathway [41–43]. The smaller Tafel slope of the RuCoMn@NC NPs indicates favorable HER kinetics. The EIS was employed to further investigate the kinetics between the electrode and electrolyte. RuCoMn@NC exhibits the smallest charge transfer resistance among all samples (Fig. 3c), indicating facilitated charge transfer. Therefore, it can promote the progress of HER. The durability of the RuCoMn@NC catalyst was evaluated by chronoamperometry. The catalyst retains 80.82% of the current density after a 10-h test (Fig. 3d). The TEM image of RuCoMn@NC after the durability test (Fig. S4) reveals that its size, morphology, and dispersion are maintained even after a long-term durability test. The C_{dl} of the catalysts was further measured by CV at a scan rate of 10–60 mV s^{-1} in a non-Faradic potential range (Fig. S5) to reflect the electrochemical surface area (ECSA) [44]. The C_{dl} of RuCoMn@NC (15.3 mF cm^{-2}) is higher than that of Co@NC (3.3 mF cm^{-2}) and RuCo@NC (2.8 mF cm^{-2}), indicating that the RuCoMn@NC catalyst has a larger electrochemical active surface area and more exposed active sites. These results demonstrate that the RuCoMn@NC NPs have excellent HER electrocatalytic activity and good stability in alkaline media.

Ideal HER electrocatalysts perform well over a wide pH range. Therefore, we further tested the HER activity of RuCoMn@NC in 0.5 mol L^{-1} H_2SO_4 and 1.0 mol L^{-1} PBS. In the 0.5 mol L^{-1} H_2SO_4 medium, RuCoMn@NC exhibits a low overpotential of 119 mV at a current density of 10 mA cm^{-2}, which is slightly higher than that of Pt/C (76 mV) but lower than that of RuCo@NC (150 mV) and Co@NC (273 mV) (Fig. 3e). The corresponding Tafel slope is 90 mV dec^{-1}, which is also higher than that of Pt/C (27 mV dec^{-1}) but lower than that of RuCo@NC (104 mV dec^{-1}) and Co@NC (122 mV dec^{-1}) (Fig. 3f). RuCoMn@NC also shows better HER performance in neutral media than in acidic media. As shown in Fig. 3g, h, RuCoMn@NC exhibits a low overpotential at 10 mA cm^{-2} (90 mV) and Tafel slope (79 mV dec^{-1}) in 1.0 mol L^{-1} PBS, which are close to those of Pt/C (82 mV and 63 mV dec^{-1}, respectively) and surpass those of RuCo@NC (254 mV and 174 mV dec^{-1}, respectively) and Co@NC (326 mV and 190 mV dec^{-1}, respectively). Overall, these results confirm that RuCoMn@NC is a potential candidate for pH-universal HER, and it outperforms the reported Ru-based electrocatalysts in alkaline solution or comparable to that in acidic and neutral solutions (Table S2). The excellent HER performance of RuCoMn@NC is superior to that of the Ru-based electrocatalysts reported so far, considering the lower overpotential, especially in alkaline media, or less content of noble metals (Table S2). To explore the possibilities of other ternary alloy systems, three other RuCo-based trimetallic electrocatalysts, including RuCoFe@NC, RuCoNi@NC, and

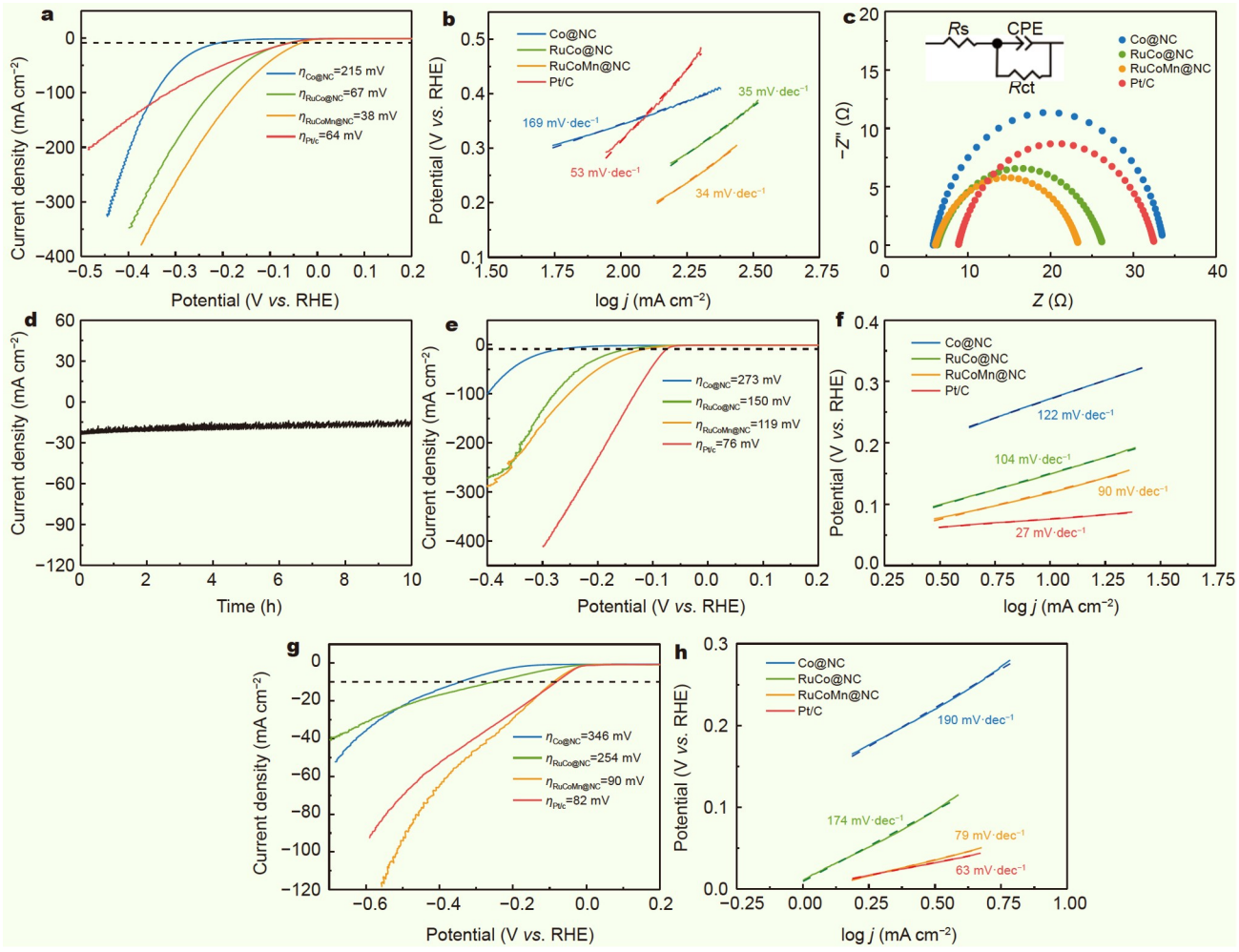

Figure 3 (a, e, g) *iR*-corrected LSV and (b, f, h) Tafel curves of RuCoMn@NC and the referenced samples in 1.0 mol L^{-1} KOH, 0.5 mol L^{-1} H_2SO_4, and 1.0 mol L^{-1} PBS for HER at a scan rate of 1 mV s^{-1} and room temperature, respectively. (c) Nyquist plots of RuCoMn@NC and the referenced samples in 1.0 mol L^{-1} KOH. (d) Time-dependent current density curve over the RuCoMn@NC catalyst during electrolysis at −0.2 V in 1.0 mol L^{-1} KOH.

RuCoCu@NC, were also synthesized *via* the same synthesis method. The samples show a similar morphology as that of RuCoMn@NC (Fig. S6). We evaluated the HER catalytic performance of the samples, and the results are shown in Fig. S7. In acidic and alkaline media, the performance of RuCoMn@NC is much higher than that of other ternary alloys, indicating that Mn is a better choice for participating in the formation of RuCo-based ternary alloy.

GOR of RuCoMn@NC catalyst

To further explore the potential of RuCoMn@NC as a redox bifunctional electrocatalyst, we evaluated the GOR activity in 1.0 mol L^{-1} KOH electrolyte using the CV technique within the scope change of potential from 0.623 to 1.423 V (*vs.* RHE) at a scan rate of 10 mV s^{-1}. Fig. 4a shows the CV curves of RuCoMn@NC, RuCo@NC, and Co@NC in the absence (black line) and presence (red line) of glucose. In the absence of glucose, the CV curve of RuCoMn@NC in the electrolyte (1.0 mol L^{-1} KOH) shows a pair of well-defined redox peaks with the anodic and cathodic peaks at around 1.20 and 1.03 V (*vs.* RHE), respectively, which can be attributed to the oxidation of tri-metal and reduction of the high valence of Co or Mn compound, respectively. After injecting glucose (concentration of glucose in alkaline solution is 3.0 mmol L^{-1}), RuCoMn@NC shows a significantly higher current increase at the anodic peak than the RuCo@NC and Co@NC electrode, suggesting that RuCoMn@NC exhibits better catalytic activity toward GOR. Furthermore, oxidation current responses increase with the concentration of glucose in the RuCoMn@NC-modified GCE (Fig. 4b), demonstrating that glucose can be easily oxidized on the surface of the catalyst over a wide concentration window. The real-time amperometric detection of glucose on the RuCoMn@NC electrode was performed by successive stepwise addition of different amounts of glucose to a KOH solution at an applied potential of 1.223 V while being stirred (Fig. 4c). As expected, the RuCoMn@NC electrode shows a steep increase in current in response to the addition of glucose, indicating the sensitive and rapid response to GOR. The corresponding curve relating to the concentration and current response is plotted (Fig. 4d). Furthermore, the plot of the electrocatalytic current of glucose *versus* its concentrations in the intercepted range of 0.02–0.4 mmol L^{-1} is shown in the inset of Fig. 4d, and the corresponding linear equation is I (μA) = 7.0672 C (mmol L^{-1}) + 4.3162, R^2 = 0.9992, with the calculated sensitivity of

36.06 μA mmol^{-1} L cm^{-2}.

Alkaline water/glucose electrolyzer

From the electrochemical characterization of HER and GOR, the RuCoMn@NC catalyst is an efficient and robust bifunctional electrocatalyst for HER and GOR in alkaline solutions. As shown in Fig. 5a, a two-electrode electrolyzer was set up using RuCoMn@NC catalyst as both cathode and anode catalyst. LSV curves of the electrolyzer using 1.0 mol L^{-1} KOH, with or without 0.1 mol L^{-1} glucose, as electrolytes are compared in Fig. 5b. With glucose, the electrolyzer exhibits a higher electrolytic current density, requiring an applied voltage of 1.63 V at a current density of 10 mA cm^{-2}, which is 270 mV less than that of the electrolyzer without glucose. Therefore, replacing OER with GOR can reduce the potential of water electrolysis.

CONCLUSIONS

In summary, we synthesized Ru-Co-Mn trimetallic alloy NPs dispersed on N-doped porous carbon polyhedra *via* the pyrolysis-adsorption-pyrolysis method using ZIF-67 as the precursor. Electrocatalytic tests show that the obtained RuCoMn@NC catalyst exhibits excellent bifunctional electrocatalytic properties for HER and GOR. The optimized RuCoMn@NC exhibits outstanding HER performance under all pH conditions, especially in alkaline media, with a low overpotential of 38 mV at 10 mA cm^{-2} in 1.0 mol L^{-1} KOH, which is

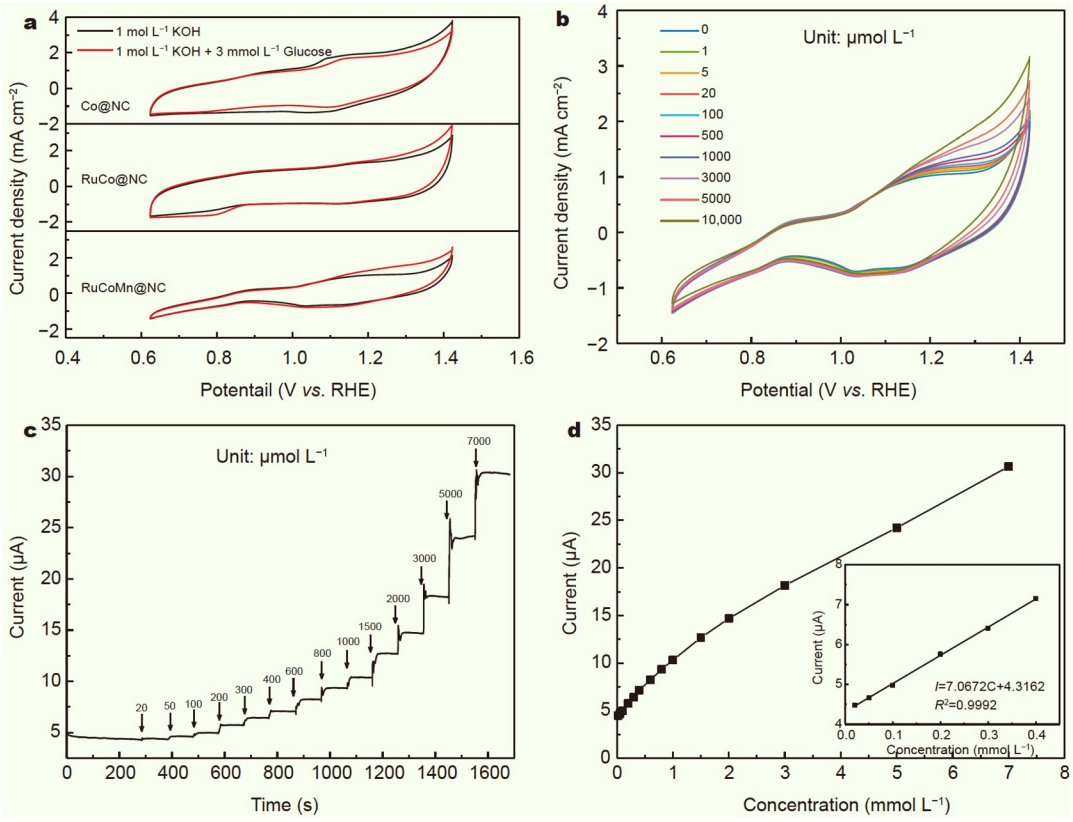

Figure 4 (a) CV curves of Co@NC, RuCo@NC, and RuCoMn@NC electrodes in the absence and presence of 3.0 mmol L^{-1} glucose in 1.0 mol L^{-1} KOH, respectively. (b) CV curves of the RuCoMn@NC electrode at different concentrations of glucose in 1.0 mol L^{-1} KOH. (c) Amperometric response of RuCoMn@NC at 1.223 V to successive addition of glucose in 1.0 mol L^{-1} KOH. (d) Corresponding curve of current *vs.* glucose concentration with fitting curve and linear range (inset).

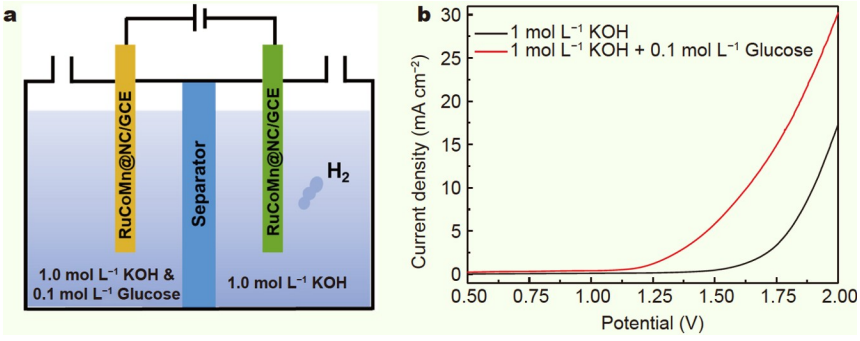

Figure 5 (a) Schematic diagram of alkaline water/glucose electrolyzer. (b) LSV plots of RuCoMn@NC in 1.0 mol L^{-1} KOH/(1.0 mol L^{-1} KOH and 0.1 mol L^{-1} glucose) with a two-electrode system.

comparable to that of Pt/C and most state-of-the-art electrocatalysts. The excellent electrocatalytic activity of RuCoMn@NC is attributed to its unique hybrid structure and composition, with the combination of alloying effect, nanoscale particle size, large surface area, abundant mesopores, and the presence of conductive N-doped carbon support. Further, a two-electrode alkaline electrolyzer device pairing RuCoMn@NC as both the cathode and anode was assembled, and it shows a low cell voltage of 1.63 V to drive the current density of 10 mA cm^{-2} in a 1.0 mol L^{-1} KOH + 0.1 mol L^{-1} glucose electrolyte. This paper would contribute to the development of highly active and robust bifunctional electrocatalysts in water electrolysis using glucose or similar organic molecules.

Received 27 April 2021; accepted 4 June 2021; published online 9 August 2021

1 Wu F, Yang H, Bai Y, *et al.* Paving the path toward reliable cathode materials for aluminum-ion batteries. Adv Mater, 2019, 31: 1806510
2 Chen J, Pan A, Zhang W, *et al.* Melamine-assisted synthesis of ultrafine Mo_2C/Mo_2N@N-doped carbon nanofibers for enhanced alkaline hydrogen evolution reaction activity. Sci China Mater, 2021, 64: 1150–1158
3 Lin C, Li H, Zhang P, *et al.* Boosting water electrolysis with anodic glucose oxidation reaction over engineered cobalt nickel hydroxide nanosheet on carbon cloth. J Electroanal Chem, 2020, 861: 113946
4 Liu X, He J, Zhao S, *et al.* Self-powered H_2 production with bifunctional hydrazine as sole consumable. Nat Commun, 2018, 9: 4365
5 Peng L, Zheng X, Li L, *et al.* Chimney effect of the interface in metal oxide/metal composite catalysts on the hydrogen evolution reaction. Appl Catal B-Environ, 2019, 245: 122–129
6 You B, Jiang N, Liu X, *et al.* Simultaneous H_2 generation and biomass upgrading in water by an efficient noble-metal-free bifunctional electrocatalyst. Angew Chem Int Ed, 2016, 55: 9913–9917
7 Jiang N, You B, Boonstra R, *et al.* Integrating electrocatalytic 5-hydroxymethylfurfural oxidation and hydrogen production *via* Co-P-derived electrocatalysts. ACS Energy Lett, 2016, 1: 386–390
8 You B, Liu X, Jiang N, *et al.* A general strategy for decoupled hydrogen production from water splitting by integrating oxidative biomass valorization. J Am Chem Soc, 2016, 138: 13639–13646
9 You B, Liu X, Liu X, *et al.* Efficient H_2 evolution coupled with oxidative refining of alcohols *via* a hierarchically porous nickel bifunctional electrocatalyst. ACS Catal, 2017, 7: 4564–4570
10 Du P, Zhang J, Liu Y, *et al.* Hydrogen generation from catalytic glucose oxidation by Fe-based electrocatalysts. Electrochem Commun, 2017, 83: 11–15
11 Rabaey K, Rozendal RA. Microbial electrosynthesis—Revisiting the electrical route for microbial production. Nat Rev Microbiol, 2010, 8: 706–716
12 Zhang E, Xie Y, Ci S, *et al.* Porous Co_3O_4 hollow nanododecahedra for nonenzymatic glucose biosensor and biofuel cell. Biosens Bioelectron, 2016, 81: 46–53
13 Gao K, Wang B, Tao L, *et al.* Efficient metal-free electrocatalysts from N-doped carbon nanomaterials: Mono-doping and Co-doping. Adv Mater, 2019, 31: 1805121
14 Zhang E, Xie Y, Ci S, *et al.* Multifunctional high-activity and robust electrocatalyst derived from metal-organic frameworks. J Mater Chem A, 2016, 4: 17288–17298
15 Cheng Z, Fu Q, Han Q, *et al.* A type of 1 nm molybdenum carbide confined within carbon nanomesh as highly efficient bifunctional electrocatalyst. Adv Funct Mater, 2018, 28: 1705967
16 Zhang Y, Wang Y, Jia S, *et al.* A hybrid of NiMo-Mo_2C/C as non-noble metal electrocatalyst for hydrogen evolution reaction in an acidic solution. Electrochim Acta, 2016, 222: 747–754
17 Feng S, Li X, Huo J, *et al.* Controllable synthesis of CoS_2@N/S-codoped porous carbon derived from ZIF-67 for as a highly efficient catalyst for the hydrogen evolution reaction. ChemCatChem, 2018, 10: 796–803
18 Vikraman D, Hussain S, Truong L, *et al.* Fabrication of MoS_2/WSe_2 heterostructures as electrocatalyst for enhanced hydrogen evolution reaction. Appl Surf Sci, 2019, 480: 611–620
19 Chu S, Chen W, Chen G, *et al.* Holey Ni-Cu phosphide nanosheets as a highly efficient and stable electrocatalyst for hydrogen evolution. Appl Catal B-Environ, 2019, 243: 537–545
20 Anandhababu G, Huang Y, Babu DD, *et al.* Oriented growth of ZIF-67 to derive 2D porous CoPO nanosheets for electrochemical-/photovoltage-driven overall water splitting. Adv Funct Mater, 2018, 28: 1706120
21 Hu G, Li J, Liu P, *et al.* Enhanced electrocatalytic activity of WO_3@NPRGO composite in a hydrogen evolution reaction. Appl Surf Sci, 2019, 463: 275–282
22 Gupta S, Patel N, Miotello A, *et al.* Cobalt-boride: An efficient and robust electrocatalyst for hydrogen evolution reaction. J Power Sources, 2015, 279: 620–625
23 Zhong H, Wang J, Zhang Y, *et al.* ZIF-8 derived graphene-based nitrogen-doped porous carbon sheets as highly efficient and durable oxygen reduction electrocatalysts. Angew Chem Int Ed, 2014, 53: 14235–14239
24 Yan D, Dou S, Tao L, *et al.* Electropolymerized supermolecule derived N, P co-doped carbon nanofiber networks as a highly efficient metal-free electrocatalyst for the hydrogen evolution reaction. J Mater Chem A, 2016, 4: 13726–13730
25 Ito Y, Cong W, Fujita T, *et al.* High catalytic activity of nitrogen and sulfur co-doped nanoporous graphene in the hydrogen evolution reaction. Angew Chem Int Ed, 2015, 54: 2131–2136
26 Qu L, Zhang Z, Zhang H, *et al.* Transformation from graphitic C_3N_4 to nitrogen-boron-carbon ternary nanosheets as efficient metal-free bifunctional electrocatalyst for oxygen reduction reaction and hydrogen evolution reaction. Appl Surf Sci, 2018, 448: 618–627
27 Meng Z, Xiao F, Wei Z, *et al.* Direct synthesis of L10-FePt nanoparticles from single-source bimetallic complex and their electrocatalytic applications in oxygen reduction and hydrogen evolution reactions. Nano Res, 2019, 12: 2954–2959
28 Azhar A, Li Y, Cai Z, *et al.* Nanoarchitectonics: A new materials horizon for Prussian blue and its analogues. Bull Chem Soc Jpn, 2019, 92: 875–904
29 Wang HF, Chen L, Pang H, *et al.* MOF-derived electrocatalysts for oxygen reduction, oxygen evolution and hydrogen evolution reactions. Chem Soc Rev, 2020, 49: 1414–1448
30 Rao CNR, Pramoda K. Borocarbonitrides, $B_xC_yN_z$, 2D nanocomposites with novel properties. Bull Chem Soc Jpn, 2019, 92: 441–468
31 Lv Y, Han M, Gong W, *et al.* Fe-Co alloyed nanoparticles catalyzing efficient hydrogenation of cinnamaldehyde to cinnamyl alcohol in water. Angew Chem Int Ed, 2020, 59: 23521–23526
32 Su J, Yang Y, Xia G, *et al.* Ruthenium-cobalt nanoalloys encapsulated in nitrogen-doped graphene as active electrocatalysts for producing hydrogen in alkaline media. Nat Commun, 2017, 8: 14969
33 Su CY, Cheng H, Li W, *et al.* Atomic modulation of FeCo-nitrogen-carbon bifunctional oxygen electrodes for rechargeable and flexible all-solid-state zinc-air battery. Adv Energy Mater, 2017, 7: 1602420
34 Sultan S, Tiwari JN, Jang JH, *et al.* Highly efficient oxygen reduction reaction activity of graphitic tube encapsulating nitrided Co_xFe_y alloy. Adv Energy Mater, 2018, 8: 1801002
35 Liu S, Wang Z, Zhou S, *et al.* Metal-organic-framework-derived hybrid carbon nanocages as a bifunctional electrocatalyst for oxygen reduction and evolution. Adv Mater, 2017, 29: 1700874
36 Zhang W, Jiang X, Wang X, *et al.* Spontaneous weaving of graphitic carbon networks synthesized by pyrolysis of ZIF-67 crystals. Angew Chem Int Ed, 2017, 56: 8435–8440
37 Gao H, Zang J, Liu X, *et al.* Ruthenium and cobalt bimetal encapsulated in nitrogen-doped carbon material derived of ZIF-67 as enhanced hydrogen evolution electrocatalyst. Appl Surf Sci, 2019, 494: 101–110
38 Ji D, Sun J, Tian L, *et al.* Engineering of the heterointerface of porous carbon nanofiber-supported nickel and manganese oxide nanoparticle for highly efficient bifunctional oxygen catalysis. Adv Funct Mater,

2020, 30: 1910568
39 Liu Q, Tian J, Cui W, *et al.* Carbon nanotubes decorated with CoP nanocrystals: A highly active non-noble-metal nanohybrid electrocatalyst for hydrogen evolution. Angew Chem Int Ed, 2014, 53: 6710–6714
40 Chen Z, Wu R, Liu Y, *et al.* Ultrafine Co nanoparticles encapsulated in carbon-nanotubes-grafted graphene sheets as advanced electrocatalysts for the hydrogen evolution reaction. Adv Mater, 2018, 30: 1802011
41 Pu Z, Amiinu IS, Kou Z, *et al.* RuP_2-based catalysts with platinum-like activity and higher durability for the hydrogen evolution reaction at all pH values. Angew Chem Int Ed, 2017, 56: 11559–11564
42 Mahmood J, Li F, Jung SM, *et al.* An efficient and pH-universal ruthenium-based catalyst for the hydrogen evolution reaction. Nat Nanotech, 2017, 12: 441–446
43 Morales-Guio CG, Stern LA, Hu X. Nanostructured hydrotreating catalysts for electrochemical hydrogen evolution. Chem Soc Rev, 2014, 43: 6555–6569
44 Šljukić B, Vujković M, Amaral L, *et al.* Carbon-supported Mo_2C electrocatalysts for hydrogen evolution reaction. J Mater Chem A, 2015, 3: 15505–15512

Acknowledgements This work was supported by the National Natural Science Foundation of China (52072035, 51631001, 21801015, 51902023 and 51872030), the Fundamental Research Funds for the Central Universities (2017CX01003), Beijing Institute of Technology Research Fund Program for Young Scholars, and the Joint R&D Plan of Hong Kong, Macao, Taiwan, and Beijing (Z191100001619002). We acknowledge the support from Beijing Zhongkebaice Technology Service Co., Ltd. for TEM and XPS characterizations.

Author contributions Liu S performed the experiments and wrote the article. Wan X, Pan R, and Su M participated in the experiments. Zhang X and Li Y performed the data analysis. Zhang E, Liu J, and Zhang J proposed the experimental design. All the authors contributed to the general discussion. All the authors have given approval to the final version of the manuscript.

Conflict of interest The authors declare that they have no conflict of interest.

Supplementary information Supporting data are available in the online version of the paper.

Shan Liu received her BE degree in 2019 from Beijing Forestry University and is currently an ME student at Beijing Institute of Technology (BIT). Her research interest focuses on composite nanomaterials and their applications in catalysis.

Erhuan Zhang received his PhD degree in 2020 from BIT and is currently a postdoctoral research fellow under the supervision of Prof. Yadong Li and Prof. Dingsheng Wang at Tsinghua University. His research interests cover advanced energy materials with a recent focus on single-atom catalysis.

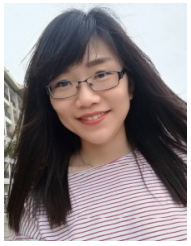

Jia Liu is currently an associate professor at the School of Materials Science and Engineering, BIT. She received her PhD degree from Dalian Institute of Chemical Physics, Chinese Academy of Sciences, in 2013. Before joining BIT in 2016, she worked as a postdoctoral research associate at the National Institute for Materials Science, Japan. Her research interests include the design and synthesis of hybrid nanocrystals for solar-to-fuel conversion systems.

Jiatao Zhang received his PhD degree in 2006 from the Department of Chemistry, Tsinghua University. Currently, he is a Xu Teli Professor at the School of Materials and Engineering, BIT. He is also the director of Beijing Key Laboratory of Construction-Tailorable Advanced Functional Materials and Green Applications. His current research interest is in the inorganic chemistry of semiconductor-based hybrid nanostructures with novel optical and electronic properties for applications in solar-to-fuel conversion, catalysis, biology, and optoelectronics devices.

双功能Ru-Co-Mn三元金属合金纳米催化剂用于氧化还原电催化

刘姗, 张二欢*, 万晓冬, 潘容容, 李岳美, 张修铭, 苏梦瑶, 刘佳*, 张加涛*

摘要 电解水是最有前景的制氢方法之一，但长期以来一直受到阳极析氧反应(OER)迟缓的限制. 本文采用热解-吸附-热解工艺，以ZIF-67为前驱体，制备了Ru-Co-Mn三金属合金纳米颗粒(NPs)负载在氮掺杂碳载体上(RuCoMn@NC)的催化剂. 该催化剂在较宽的pH范围内对析氢反应(HER)以及在碱性介质中对葡萄糖氧化反应(GOR)都表现出良好的电催化性能. 特别是RuCoMn@NC催化剂在碱性介质中表现出优异的HER活性，优于商用Pt/C催化剂(20 wt%)，并具有良好的电化学稳定性. 进一步以RuCoMn@NC同时作为阴极和阳极组成双电极碱性电解槽用于葡萄糖电解反应，只需要1.63 V的槽电压就可以达到10 mA cm^{-2}的电流密度，比全解水电解槽的所需电压低270 mV. 本工作为合理开发高效的氧化还原电催化双功能催化剂提供了一种有效的方法，有利于节能电解制氢的发展.

